

Communication

# Binder-Free $\text{CoMn}_2\text{O}_4$ Nanoflower Particles/Graphene/Carbon Nanotube Composite Film for a High-Performance Lithium-Ion Battery

Xin Tong<sup>1,\*</sup>, Bo Yang<sup>1,†</sup>, Fei Li<sup>2</sup>, Manqi Gu<sup>1</sup>, Xinxing Zhan<sup>1</sup>, Juan Tian<sup>1</sup>, Shengyun Huang<sup>3,\*</sup> and Gang Wang<sup>2,\*</sup><sup>1</sup> School of Chemistry and Material Science, Guizhou Normal University, Guiyang 550001, China<sup>2</sup> State Key Laboratory of Photon-Technology in Western China Energy, Institute of Photonics & Photon-Technology, Northwest University, Xi'an 710127, China<sup>3</sup> Ganjiang Innovation Academy, Chinese Academy of Sciences, Ganzhou 341000, China

\* Correspondence: tongxin@gznu.edu.cn (X.T.); shyhuang@gia.cas.cn (S.H.); gangwang@nwu.edu.cn (G.W.)

† These authors contributed equally to this work.

**Abstract:** Manganese-based bimetallic oxides show a high theoretical specific capacity, making them a potential next-generation lithium-ion battery anode material. However, as with metal oxide anode materials, aggregation, volume expansion, and poor conductivity are the main obstacles. In this manuscript, flexible  $\text{CoMn}_2\text{O}_4$ /graphene/carbon nanotube films were successfully prepared through a facile filtration strategy and a subsequent thermal treatment process. When used as anodes for lithium batteries, these films can be pressed onto nickel foam without other conductive additives and binders, which simplifies the manufacturing process. When used as an anode in the lithium-ion battery,  $\text{CoMn}_2\text{O}_4$ /GR/CNT film exhibits a high discharge capacity of  $881 \text{ mAh g}^{-1}$  after 55 cycles. This value is  $\sim 2$  times higher than the discharge capacity of  $\text{CoMn}_2\text{O}_4$ . The three-dimensional GR/CNT carrier effectively dispersed  $\text{CoMn}_2\text{O}_4$ , preventing its aggregation and alleviating the problem of volume expansion.

**Keywords:** lithium-ion battery; anode materials;  $\text{CoMn}_2\text{O}_4$  nanoflower; graphene; film

**Citation:** Tong, X.; Yang, B.; Li, F.; Gu, M.; Zhan, X.; Tian, J.; Huang, S.; Wang, G. Binder-Free  $\text{CoMn}_2\text{O}_4$  Nanoflower Particles/Graphene/Carbon Nanotube Composite Film for a High-Performance Lithium-Ion Battery. *Inorganics* **2023**, *11*, 314.

<https://doi.org/10.3390/inorganics11080314>

Academic Editors: Roberto Nisticò, Torben R. Jensen, Luciano Carlos, Hicham Idriss and Eleonora Aneggi

Received: 17 May 2023  
Revised: 19 July 2023  
Accepted: 23 July 2023  
Published: 25 July 2023



**Copyright:** © 2023 by the authors. Licensee MDPI, Basel, Switzerland. This article is an open access article distributed under the terms and conditions of the Creative Commons Attribution (CC BY) license (<https://creativecommons.org/licenses/by/4.0/>).

## 1. Introduction

The development and progress of society have made people heavily dependent on fossil fuels. However, this dependence has led to energy depletion and serious environmental pollution problems. Exploring various devices for efficient energy storage and conversion is crucial to enable the effective use of energy. In recent years, lithium-ion batteries (LIBs) have received extensive attention due to their large capacity, high power density, and good cycle stability. LIBs have emerged as critical power sources for a wide range of applications, including portable electronics and electric vehicles [1]. As demand for these devices continues to grow, it is crucial to improve their energy density, rapid charge capability, power density, as well as their durability [2–4]. Research on lithium-ion batteries has focused on developing electrode materials with higher capacity, greater safety, and lighter weight. Unfortunately, the current anode materials, such as graphite and carbon-based electrode materials, are unable to meet these requirements due to their poor rate capability and low theoretical capacity [5,6]. To overcome this technological bottleneck, high-performance anode materials are required.

Numerous micro-/nano-structured metal oxides have garnered significant attention as potential anode materials due to their high energy density. In recent decades, transition metal oxides (TMOs) have gained significant attention due to their structural diversity and unique electron transport properties that result from the properties of the outer d electrons. They offer promising applications in various fields such as spintronics and thermoelectrics [7–9]. As research continues, complex transition metal oxides, with a general

formula of  $X_xY_{3-x}O_4$  ( $X, Y = \text{Fe, Co, Ni, Zn, Mn, etc.}$ ), have emerged as superior alternatives. Binary transition metal oxides typically adopt a spinel structure. By incorporating additional transition metals, more active sites can be introduced and the crystal structure and valence state of any metal element can be optimized. The synergistic effect of the two metal oxides during charging and discharging, along with the attractive interactions between different cations, can facilitate a greater number of redox reactions. Consequently, binary transition metal oxides exhibit higher reversible storage capacity and enhanced electronic conductivity compared with single metal oxides [10]. This excellent electrochemical activity positions them with great potential for energy storage and conversion applications [11]. Among various transition metal oxide materials, manganese-based oxides have garnered considerable attention due to their lower operating voltage and higher energy density. For instance, Yu et al. employed a simple solvothermal and thermal treatment process to grow hierarchical  $\text{CoM}_{3-x}\text{O}_4$  arrays/nanostructures on stainless steel substrates [12]. By adjusting the volume ratio of solvent,  $\text{CoMn}_2\text{O}_4$  nanowires and  $\text{MnCo}_2\text{O}_4$  nanosheets were synthesized. The layered structure of these materials facilitates contact between the electroactive surface and the electrolyte, resulting in excellent electrochemical properties and cycling stability. In particular, the  $\text{CoMn}_2\text{O}_4$  material, with its combination of cobalt's high oxidation potential and manganese's high capacity and excellent electron transport properties, exhibits great promise as an anode material for lithium-ion batteries [13]. However, their commercial application is hindered by inferior cycling stability and poor rapid charge capability, which are possibly due to sluggish electronic/ionic diffusion and unsatisfactory structural stability.

To address these issues, many strategies have been attempted. One useful method is to build different nanostructures from transition metal oxides using various strategies such as hierarchical mesoporous microspheres [14], hollow nanospheres [15], yolk-shell microspheres [16], hollow nanofibers [17], and bubble-like structures [18]. Hu et al. prepared hierarchical mesoporous  $\text{CoMn}_2\text{O}_4$  microspheres using a facile solvothermal carbon templating method [14]. This material exhibited excellent cycling stability and high discharge capacity due to its unique hierarchical structure, which enhances electrolyte diffusion, shortens the  $\text{Li}^+$  ion diffusion length, and accommodates volume-change-induced strain during cycling. Zhou et al. reported the synthesis of double-shell  $\text{CoMn}_2\text{O}_4$  hollow microcubes using a co-precipitation and thermal annealing method [19]. The unique structure allowed the synthesized  $\text{CoMn}_2\text{O}_4$  material to have a reversible capacity of  $830 \text{ mA h g}^{-1}$  at a current density of  $200 \text{ Ag}^{-1}$ . A discharge capacity of  $406 \text{ mA h g}^{-1}$  was still maintained after 50 cycles at  $800 \text{ mA g}^{-1}$ , demonstrating excellent cycling performance. Another important strategy is to combine TMOs with conductive carbon materials, especially graphene [20], nitrogen-doped graphene [21], and carbon hollow spheres [22]. The introduction of carbon materials not only provides high electrical conductivity but also serves as a support material to alleviate the volume expansion of the metal oxide for energy application. Cai et al. have synthesized a composite material consisting of  $\text{CoMn}_2\text{O}_4$  nanoparticles anchored on reduced graphene oxide (rGO) sheets [23]. The rGO can prevent the aggregation of  $\text{CoMn}_2\text{O}_4$  nanoparticles, which could otherwise reduce the active surface area of the cathode material and limit its performance. Furthermore, the flexible and porous structure of rGO can help to build a suitable flexible carbon matrix [24], allowing the material to accommodate the volume change that occurs during the charging and discharging of the battery, while also improving the electrical conductivity of the cathode material. This is important for maintaining the stability and performance of the battery over repeated charge–discharge cycles. To explore high-performance transition metal oxide electrodes, the rational design of the material's structure is essential. In the preparation of electrodes, the nature of the binder directly affects the electrochemical properties of transition metal oxides. Conventional electrodes are used by mixing electroactive materials with an insulating polymer binder and coating them on the collector. The ratio and distribution of the binder directly impact performance. Compositing transition metals with conductive materials avoids the use of binders. With this structure, the weight is reduced while exposing more active sites and the

electrode can directly contact the electrolyte better, exhibiting satisfactory lithium storage performance [25,26].

In this manuscript, the  $\text{CoMn}_2\text{O}_4$  nanoflower particles are synthesized by hydrothermal method. Then one-dimensional carbon nanotube (CNT) and two-dimensional graphene (GR) are used to build a three-dimensional network structure of GR/CNT to support the  $\text{CoMn}_2\text{O}_4$  nanoflower particles. The  $\text{CoMn}_2\text{O}_4/\text{GR}/\text{CNT}$  composite film not only has the potential to improve the overall conductivity of the material but also effectively alleviate volume expansion and aggregation problems.

## 2. Experimental Section

### 2.1. Preparation of $\text{CoMn}_2\text{O}_4$

A total of 0.33 g of polyvinylpyrrolidone, 1.5 mmol of  $\text{Co}(\text{CH}_3\text{COO})_2$ , and 3 mmol of  $\text{Mn}(\text{CH}_3\text{COO})_2$  were sequentially added into a mixed solution consisting of 90 mL of ethylene glycol and 1.5 mL of deionized water. After moderate stirring, the resulting homogeneous solution was transferred into two 50 mL hydrothermal autoclaves, heated to 180 °C, and maintained for 12 h [27]. Upon cooling to room temperature naturally, the product was obtained by washing with ethanol through centrifugation and drying in a vacuum at 60 °C for 12 h. Finally, the dried powder was heated from room temperature to 500 °C at a rate of 1 °C/min under ambient atmosphere and calcined at this temperature for 4 h. The obtained black powder is referred to as  $\text{CoMn}_2\text{O}_4$ .

### 2.2. Fabrication of $\text{CoMn}_2\text{O}_4/\text{GR}/\text{CNT}$ Composite Film

The preparation of graphene oxide (GO) was achieved using an improved Hummers method [28] through a three-step process: low-temperature oxidation, high-temperature oxidation, and hydrolysis. Firstly, 1 g of graphite powder provided by the China National Pharmaceutical Group Co. was added to a mixture of 92 mL of concentrated sulfuric acid (95–98%) and 24 mL of nitric acid (65%) in a 500 mL flask placed in an ice bath. The suspended solution was vigorously stirred at 0 °C for 1h, constituting the low-temperature oxidation process. Next, to further enhance the oxidation degree of the graphite, the mixture was heated to 80 °C for 30 min, representing the high-temperature oxidation step. Following that, 92 mL of deionized water was slowly added and the suspension was stirred at 80 °C for an additional 30 min, concluding the hydrolysis process. Afterward, to reduce the remaining permanganate, 5 mL of  $\text{H}_2\text{O}_2$  (30%) was added to the solution. Upon completion of the reaction, the resulting mixture was washed with a 5% solution of HCl and water until no sulfate was detected with  $\text{BaCl}_2$ . Finally, the GO powders were dried at 80 °C for 24 h, completing the post-treatment steps of drying and washing. The GO (20 mg) and the carbon nanotube (CNT) (10 mg) provided by Zhongke Times Nanomaterials Co., Ltd. were dispersed in 10 mL of deionized water by ultrasonication. The resulting suspension was stirred continuously for 12 h on a magnetic stirrer after adding 20 mg of the as-prepared  $\text{CoMn}_2\text{O}_4$ . The suspension was then transferred to a vacuum filtration apparatus (1000 mL) and continuously filtered for 4 h. The resulting thin film was transferred to a petri dish and briefly soaked in acetone solution. The synthesized thin film was then quickly peeled off from the microporous membrane using forceps. Finally, the peeled thin film was calcined at 220 °C for 2 h and the resulting  $\text{CoMn}_2\text{O}_4/\text{GR}/\text{CNT}$  composite film was synthesized.

### 2.3. Characterization

The surface composition of the samples was analyzed by X-ray diffraction (XRD) patterns using a Bruker D8 ADVANCE X-ray diffractometer equipped with a  $\text{Cu-K}\alpha$  radiation source and scanning ranges of 2–10° and 10–70°. The scanning electron microscopy (SEM) images were obtained using an FEI Quanta 400 ESEM-FEG instrument with an accelerating voltage of 20–40 kV.

#### 2.4. Electrochemical Measurements

Foam nickel was used as the current collector, and the prepared thin film material was cut into appropriate sizes and pressed into electrode plates using a powder press machine at 20 MPa. The loading amount of the active substance on each electrode plate was approximately  $2 \text{ mg cm}^{-2}$ . The electrode plates were used as the working electrode, lithium foil as the counter and reference electrode, and polypropylene porous membrane (Celgard2400) as the separator. The electrolyte was 1 M  $\text{LiPF}_6$ /ethylene carbonate–dimethyl carbonate–methyl carbonate (EC-DMC-EMC) with a volume ratio of 1:1:1. The energy storage characteristics of the battery materials, such as specific capacity, rate performance, cycle life, and Coulomb efficiency, were mainly evaluated through charge and discharge cycle tests. The battery testing system used in this manuscript was produced by Wuhan LAND Electronic Technology Co., Ltd. The test conditions were a constant temperature of  $30^\circ\text{C}$ , a voltage range of 0–3.0 V, and a current density of 50–1600 mA/g to complete the charge and discharge cycle tests. Cyclic voltammetry (CV) was performed using the CS310 electrochemical workstation produced by Wuhan KEJIA Technology Co., Ltd, Wuhan, China. The CV test conditions were a voltage range of 0–3.0 V and a scan rate of 0.2 mV/s.

### 3. Results and Discussion

Figure 1 illustrates the fabrication process of the  $\text{CoMn}_2\text{O}_4/\text{GR}/\text{CNT}$  composite film. In a typical experiment,  $\text{CoMn}_2\text{O}_4$  nanoflower particles were initially synthesized using a hydrothermal method. This process involved the controlled reaction between specific precursor materials under suitable temperature and pressure conditions, resulting in the formation of the  $\text{CoMn}_2\text{O}_4$  nanoflowers. Next, two-dimensional graphite oxide (GO) and one-dimensional carbon nanotube (CNT) were dispersed in deionized water and mixed with the  $\text{CoMn}_2\text{O}_4$  nanoflowers. The mixture was stirred for 12 h to ensure a homogeneous distribution of the nanomaterials and promote the interaction between the components. The resulting suspension, containing the  $\text{CoMn}_2\text{O}_4$  nanoflowers, GO, and CNT, was then subjected to vacuum filtration. This process involved filtering the suspension through a porous membrane, resulting in the formation of a thin brown film on the membrane surface. Subsequently, the film was calcined at  $220^\circ\text{C}$  for 2 h to remove any residual oxygen group and promote the formation of strong interfacial bonds between the components. The calcination process led to the formation of the final black product, which represents the  $\text{CoMn}_2\text{O}_4/\text{GR}/\text{CNT}$  composite film. The integration of the  $\text{CoMn}_2\text{O}_4$  nanoflower particles within the three-dimensional network structure of GR and CNT provides several advantages. Firstly, the GR/CNT network offers a large surface area, allowing for enhanced interaction and efficient utilization of the active materials. Secondly, the presence of CNT and GR improves the overall electrical conductivity of the composite, facilitating rapid charge and ion transport within the electrode material.

To analyze the structure of the  $\text{CoMn}_2\text{O}_4/\text{GR}/\text{CNT}$  film and evaluate the impact of the incorporation of GR/CNT on  $\text{CoMn}_2\text{O}_4$ , SEM characterization was conducted. Figure 2a,b present SEM images of the carbon nanotube (CNT) and graphene (GR). The SEM image of the CNT (Figure 2a) reveals a distinctive tubular structure with a curved morphology. The CNT exhibit a range of orientations, intertwining and interconnecting with each other. Moreover, in Figure 2b, the graphene displays a layered two-dimensional arrangement, demonstrating a stacked structure. The graphene layers are stacked on top of each other, creating a layered configuration with well-defined boundaries between the individual graphene sheets. Figure 2c,d show SEM images of pure  $\text{CoMn}_2\text{O}_4$  and  $\text{CoMn}_2\text{O}_4/\text{GR}/\text{CNT}$  composite films at different magnifications. It can be observed from Figure 2c,d that without the introduction of GR/CNT,  $\text{CoMn}_2\text{O}_4$  aggregates severely. From the high-magnification SEM image in Figure 2c, it can be seen that the prepared  $\text{CoMn}_2\text{O}_4$  is composed of porous nanosheets, forming nanoflowers that have diameters of about 300 nm. Figure 2e,f show SEM images of  $\text{CoMn}_2\text{O}_4/\text{GR}/\text{CNT}$  composite films. The material with a sheet-like structure is graphene, whereas the material with a curved and fluffy structure is the carbon nanotube (CNT). The graphene sheets formed a three-dimensional

framework that supported the  $\text{CoMn}_2\text{O}_4$  particles, whereas the long and curved carbon nanotube filled the gaps between the graphene sheets and between  $\text{CoMn}_2\text{O}_4$  particles and graphene sheets, facilitating connectivity between the  $\text{CoMn}_2\text{O}_4$  and graphene. It can be seen that after vacuum filtration and heat treatment, the shape of  $\text{CoMn}_2\text{O}_4$  nanoflowers did not change, and they were uniformly embedded in the GR/CNT composite film. The existence of the 3D structure of GR/CNT effectively mitigated the phenomenon of  $\text{CoMn}_2\text{O}_4$  nanoflower particle aggregation compared with Figure 2e. The CNT in the film can effectively compensate for the defect of poor conductivity in the GR layer.

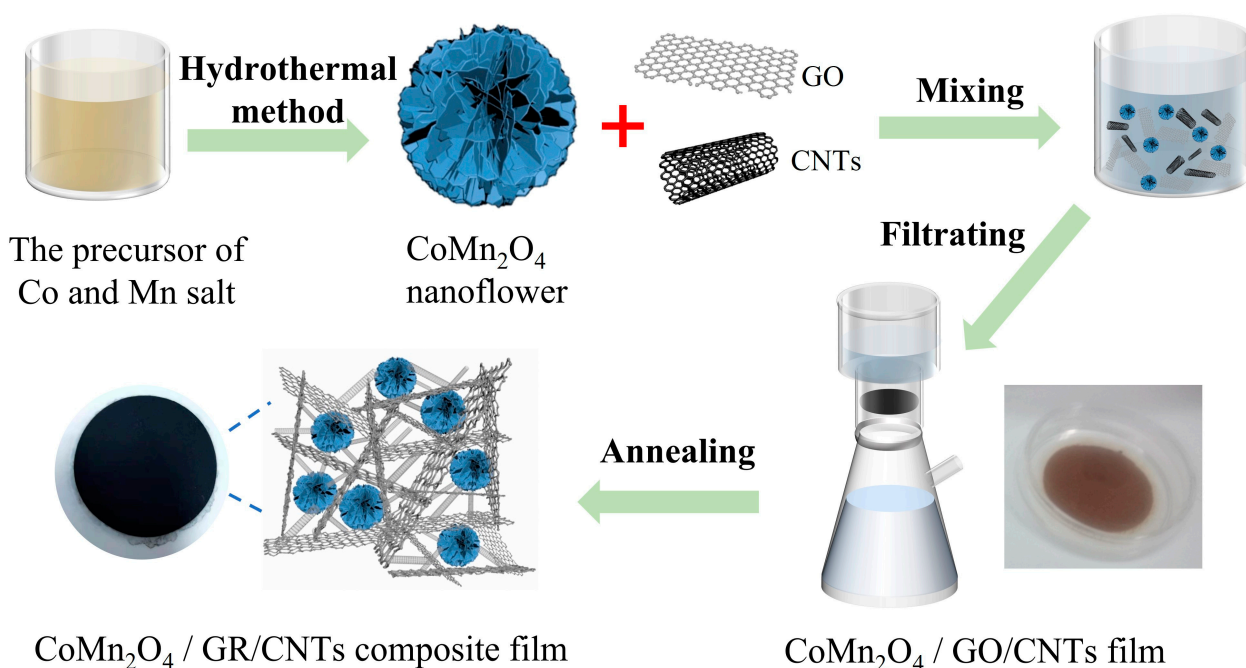


**Figure 1.** Schematic diagram of  $\text{CoMn}_2\text{O}_4$  nanoflower particles/graphene/carbon nanotube composite film.

To determine the phase composition of the as-prepared materials, X-ray diffraction (XRD) analysis were carried out on the as-synthesized GR,  $\text{CoMn}_2\text{O}_4$  microflowers, and the  $\text{CoMn}_2\text{O}_4$ /GR/CNT composite film. Figure 3a shows the low-angle X-ray diffraction (XRD) patterns of the as-prepared materials within the range of  $2\text{--}10^\circ$ . Upon analysis of the XRD patterns, it was observed that the GR exhibits a relatively featureless pattern in this low-angle range, with no distinct peaks observed. This indicates the amorphous nature or very fine crystalline structure of the graphene. In contrast, the  $\text{CoMn}_2\text{O}_4$  nanoflower particles exhibit a characteristic peak at approximately  $2.46^\circ$ , suggesting the presence of a crystalline phase in the material. Interestingly, in the XRD pattern of the  $\text{CoMn}_2\text{O}_4$ /GR/CNT composite film, a peak is observed at the same position as the  $\text{CoMn}_2\text{O}_4$  nanoflower particles. However, this peak appears to be slightly broadened compared with the pure  $\text{CoMn}_2\text{O}_4$ , indicating a potential modification in the crystalline structure or an influence from the presence of GR and CNT. From the wide-angle XRD diffractogram of GR in Figure 3b, it is evident that a diffraction peak is observed around  $25^\circ$ , which corresponds to the (002) crystal plane of graphene. This peak signifies that GR possesses an amorphous structure with no prominent crystalline peaks observed within the low-angle range of  $2\text{--}10^\circ$ . The pure  $\text{CoMn}_2\text{O}_4$  nanoflowers (represented by the green line) showed diffraction peaks at  $2\theta = 18.2^\circ, 29.3^\circ, 31.2^\circ, 32.9^\circ, 36.4^\circ, 4.8^\circ, 59.0^\circ$ , and  $60.7^\circ$ , corresponding to the (111), (202), (220), (113), (311), (400), (511), and (404) crystal faces, respectively, consistent with the PDF card (JCPDS 23-1237), with no other impurity peaks appearing, indicating the high purity of  $\text{CoMn}_2\text{O}_4$ . The brown line in Figure 3 represents the  $\text{CoMn}_2\text{O}_4$ /GR/CNT film. In the  $\text{CoMn}_2\text{O}_4$ /GR/CNT composites, some of the XRD peaks have become broader and less

distinct. This could be attributed to the introduction of graphene and carbon nanotube that could have caused some lattice distortion and reduced the crystallinity of the  $\text{CoMn}_2\text{O}_4$  nanoparticles. However, the main diffraction peaks of  $\text{CoMn}_2\text{O}_4$  were still identifiable, indicating that the introduction of GR/CNT did not significantly affect the crystal structure of  $\text{CoMn}_2\text{O}_4$ .

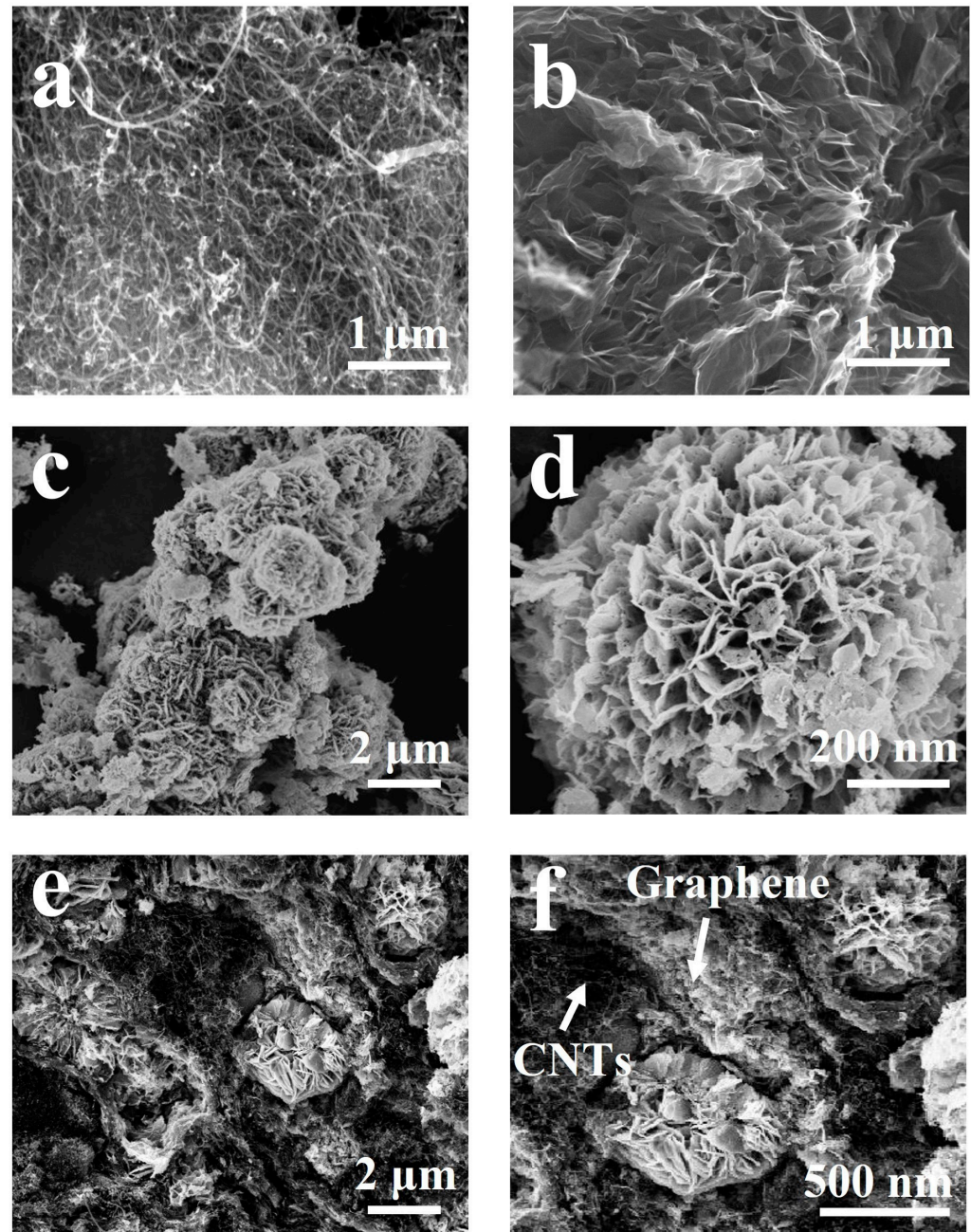


**Figure 2.** The SEM images of as-prepared (a,b) CNT and GR, (c,d)  $\text{CoMn}_2\text{O}_4$  nanoflower particles, and (e,f)  $\text{CoMn}_2\text{O}_4$ /GR/CNT composite film.

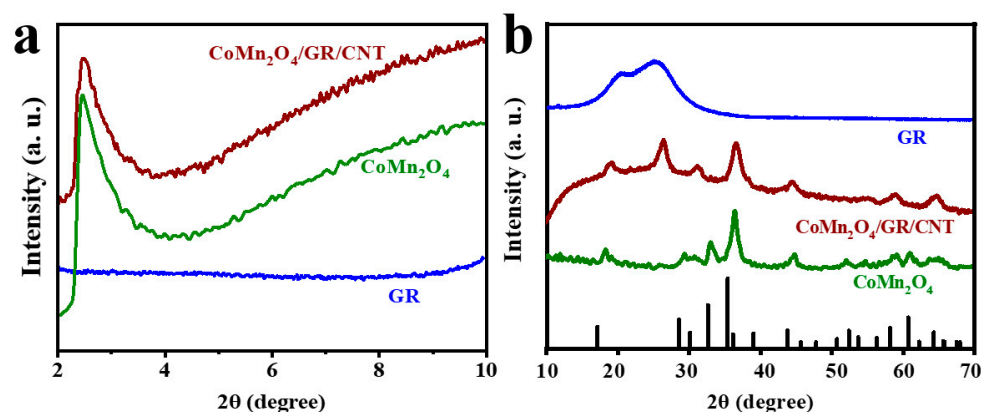


**Figure 3.** (a) Low-angle and (b) wide-angle X-ray diffraction (XRD) patterns of as-prepared GR,  $\text{CoMn}_2\text{O}_4$  nanoflower particles, and  $\text{CoMn}_2\text{O}_4/\text{GR}/\text{CNT}$  composite film.

The cyclic voltammetry (CV) technique was used to study the electrochemical behavior of the  $\text{CoMn}_2\text{O}_4/\text{GR}/\text{CNT}$  composites. Figure 4a illustrates the cyclic voltammetry (CV) curves of the composite film electrode during the first three cycles. The CV curve of the initial cycle exhibits a distinct difference compared with the subsequent two cycles, particularly in the reduction curve. During the initial lithiation process, a broad reduction peak appears at 1.25 V, which is mainly attributed to the reduction of  $\text{Co}^{3+}$  to  $\text{Co}^{2+}$ . The sharp peak at 0.4 V is attributed to the transformation of  $\text{Co}^{2+}$  and  $\text{Mn}^{2+}$  to metal Co and Mn. The two peaks at 1.65 V and 2.0 V in the delithiation process are attributed to the oxidation of metal Co and Mn to  $\text{Co}^{2+}$  and  $\text{Mn}^{2+}$ . In the subsequent cycles, the peaks at 0.45/1.65 V and 1.1 V/2.0 V represent the repetitive reduction/oxidation of MnO and CoO, respectively [14]. Figure 4b shows the first three charge/discharge curves of the  $\text{CoMn}_2\text{O}_4/\text{GR}/\text{CNT}$  composite electrode at a current density of  $100 \text{ mA g}^{-1}$ . It can be seen from the figure that the initial specific capacities of  $\text{CoMn}_2\text{O}_4/\text{GR}/\text{CNT}$  for charge and discharge are  $1164/2148 \text{ mAh g}^{-1}$ , respectively. Due to the irreversible formation of SEI film during the first charge/discharge cycle, a part of  $\text{Li}^+$  is lost, resulting in a low coulombic efficiency of 54%.

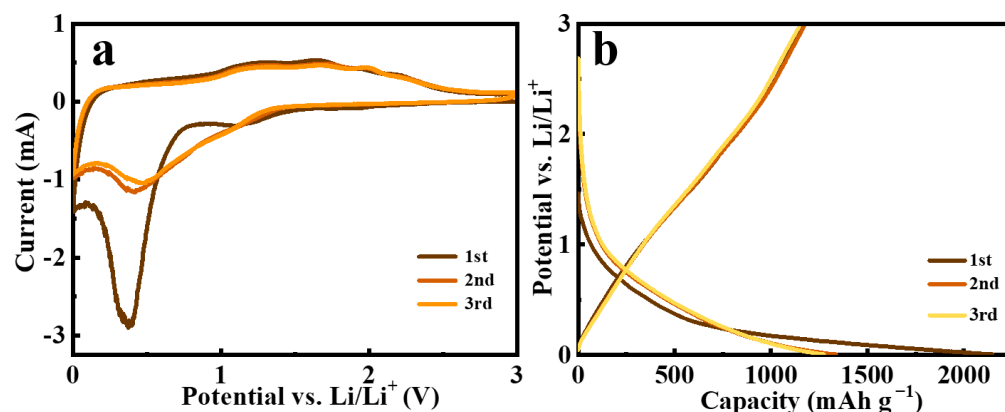


**Figure 4.** Electrochemical performance of  $\text{CoMn}_2\text{O}_4/\text{GR}/\text{CNT}$  film for LIBs at room temperature ( $25^\circ\text{C}$ ). (a) Cyclic voltammograms between 0.0 V and 3.0 V at a scan rate of  $0.1 \text{ mV s}^{-1}$  for the initial three cycles. (b) Charge–discharge voltage profiles at a current density of  $0.1 \text{ A g}^{-1}$  for the initial three cycles.

A galvanostatic charge–discharge test was conducted to further evaluate the electrochemical performance of the  $\text{CoMn}_2\text{O}_4$  and  $\text{CoMn}_2\text{O}_4/\text{GR}/\text{CNT}$  composite film electrodes. The cycling performance of  $\text{CoMn}_2\text{O}_4$  and  $\text{CoMn}_2\text{O}_4/\text{GR}/\text{CNT}$  at a current density of  $100 \text{ mA g}^{-1}$  for the first 55 cycles is presented in Figure 5a. The initial discharge specific capacities of the  $\text{CoMn}_2\text{O}_4$  and  $\text{CoMn}_2\text{O}_4/\text{GR}/\text{CNT}$  films were 1514 and

2148 mAh g<sup>-1</sup>, respectively. Although the difference in specific capacity between CoMn<sub>2</sub>O<sub>4</sub> and CoMn<sub>2</sub>O<sub>4</sub>/GR/CNT films was not significant during the first few cycles, the discharge specific capacity of the CoMn<sub>2</sub>O<sub>4</sub> electrode decreased rapidly with increasing cycle number. After 55 cycles, the discharge specific capacity of the CoMn<sub>2</sub>O<sub>4</sub> electrode was only 457 mAh g<sup>-1</sup>, which was about half of that of the CoMn<sub>2</sub>O<sub>4</sub>/GR/CNT material (881 mAh g<sup>-1</sup>) under the same testing conditions. The discharge specific capacity of CoMn<sub>2</sub>O<sub>4</sub>/GR/CNT composites decreases very slowly and reaches a stable plateau after about 15 cycles. The enhanced electrochemical performance can be attributed to the synergistic effect of the three-dimensional network structure of GR/CNT and the highly dispersed CoMn<sub>2</sub>O<sub>4</sub> nanoflowers, which provides a large surface area and efficient electron and ion transport pathways. Furthermore, the introduction of GR/CNT effectively alleviates the volume expansion and agglomeration of CoMn<sub>2</sub>O<sub>4</sub> during the charge–discharge process, maintaining the integrity and activity of CoMn<sub>2</sub>O<sub>4</sub> during the stability test.

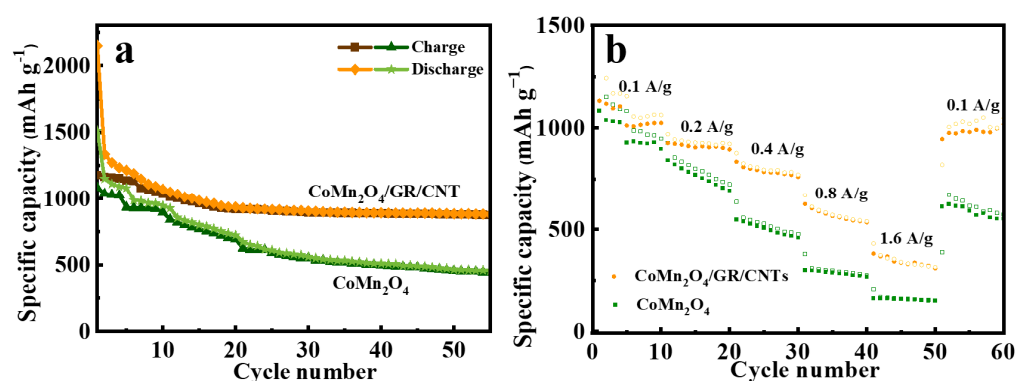


**Figure 5.** Electrochemical performance of CoMn<sub>2</sub>O<sub>4</sub> and CoMn<sub>2</sub>O<sub>4</sub>/GR/CNT film for LIBs at room temperature (25 °C). (a) Cycling performance. (b) Rate capability at various current rates.

Figure 5b displays the rate performance curves of the CoMn<sub>2</sub>O<sub>4</sub> and CoMn<sub>2</sub>O<sub>4</sub>/GR/CNT electrodes tested at current densities of 100, 200, 400, 800, and 1600 mA g<sup>-1</sup>. In the tested conditions with current densities of 100, 200, 400, 800, and 1600 mA g<sup>-1</sup>, the average discharge specific capacities of CoMn<sub>2</sub>O<sub>4</sub> were found to be 1082, 800, 528, 296, and 161 mA g<sup>-1</sup>, respectively. However, when the current density was suddenly reduced to 100 mA g<sup>-1</sup>, the discharge specific capacity of the CoMn<sub>2</sub>O<sub>4</sub> electrode could only recover to 616 mA g<sup>-1</sup>. In contrast, under the same testing conditions, the average discharge specific capacities of the CoMn<sub>2</sub>O<sub>4</sub>/GR/CNT composite films were 1155, 923, 796, 572, and 339 mA g<sup>-1</sup>, and when the current density was reduced to 100 mA g<sup>-1</sup> again, the discharge specific capacity could be restored to the original level, reaching 1020 mA g<sup>-1</sup>. The rate performance of the unmodified CoMn<sub>2</sub>O<sub>4</sub> material is not satisfactory and its capacity decay is relatively rapid, especially after experiencing high current density charge–discharge. Furthermore, at any given current density, the specific capacity of the CoMn<sub>2</sub>O<sub>4</sub>/GR/CNT electrode is higher than that of the CoMn<sub>2</sub>O<sub>4</sub> electrode, indicating that the introduction of GR/CNT has led to the better rate performance of the CoMn<sub>2</sub>O<sub>4</sub>/GR/CNT electrode. This suggests that the introduction of GR/CNT can provide a conductive network and increase the electron transfer rate, which can effectively alleviate the polarization effect and improve the rate performance of the CoMn<sub>2</sub>O<sub>4</sub>/GR/CNT electrode.

The CoMn<sub>2</sub>O<sub>4</sub>/GR/CNT composite film has shown improved performance in lithium-ion batteries (LIBs); this is mainly attributed to its unique structure. As shown in Figure 6, the CoMn<sub>2</sub>O<sub>4</sub> nanoparticles are embedded in the three-dimensional network structure of the GR/CNT matrix, forming a continuous and porous conductive network. The GR sheets and CNT can not only provide good electrical conductivity but also prevent the aggregation of CoMn<sub>2</sub>O<sub>4</sub> nanoparticles during the charge–discharge process, which can effectively improve the structural stability of the electrode and enhance the rate performance. Moreover, the CoMn<sub>2</sub>O<sub>4</sub> particles in the composite film are distributed uniformly

on the surface of the graphene and carbon nanotube, which increases the electrode's specific surface area and enhances the interaction between the electrode and electrolyte. This enhanced interaction can facilitate the diffusion of lithium ions and improve the electrode's electrochemical performance. In addition, the composite film also shows improved rate capability due to the enhanced conductivity and the reduced diffusion length of lithium ions in the electrode material. The conductive network provided by the GR and CNT can facilitate the movement of  $\text{Li}^+$  ions and electrons in the electrode material, whereas the smaller diffusion length of lithium ions in the  $\text{CoMn}_2\text{O}_4$  particles can improve the rate capability of the electrode.

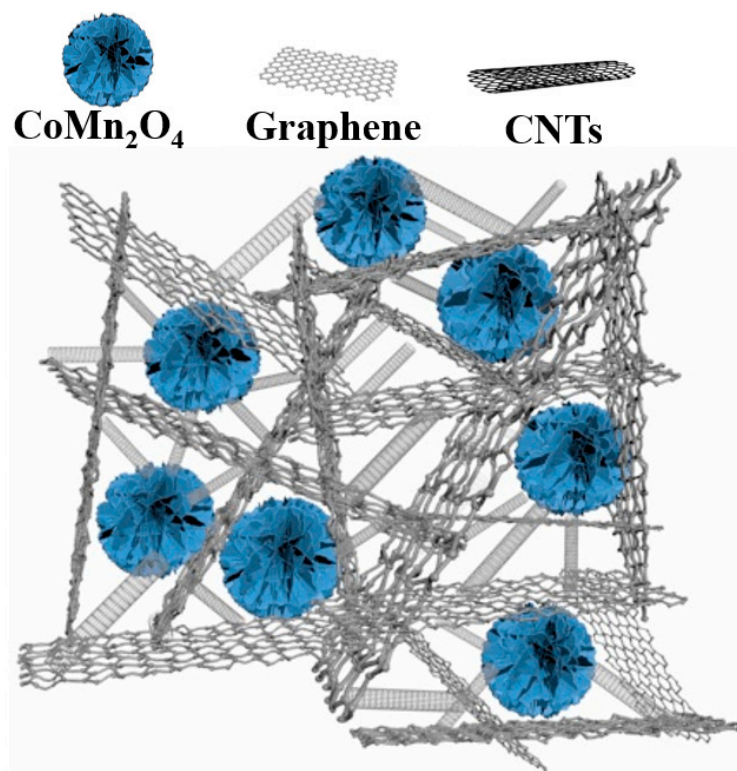


**Figure 6.** Schematic illustration of  $\text{CoMn}_2\text{O}_4$ /graphene/carbon nanotube composite film-based anode.

#### 4. Conclusions

In summary, the  $\text{CoMn}_2\text{O}_4$ /graphene/carbon nanotube composite film was successfully prepared via a facile vacuum filtrating method and demonstrated improved performance as an anode material for lithium-ion batteries. The  $\text{CoMn}_2\text{O}_4$ /GR/CNT composite film exhibited a high initial discharge capacity of  $2148 \text{ mAh g}^{-1}$  and superior cycle stability ( $881 \text{ mAh g}^{-1}$  after 55 cycles) compared with the unmodified  $\text{CoMn}_2\text{O}_4$  film. The composite film also demonstrated better rate performance, with a higher average discharge capacity at various current densities. The results suggest that the  $\text{CoMn}_2\text{O}_4$ /graphene/carbon nanotube composite film is a promising anode material candidate for high-performance lithium-ion batteries. The addition of graphene and carbon nanotube to the  $\text{CoMn}_2\text{O}_4$  film improved its conductivity and provided structural support, which effectively reduced volume expansion and aggregation during the charge and discharge process, thus maintaining the integrity and activity of the  $\text{CoMn}_2\text{O}_4$  material. This study highlights the importance of designing and developing advanced materials for energy storage applications and the potential of using graphene and carbon nanotube as effective additives to improve the performance of metal-oxide-based anode materials in lithium-ion batteries.

In addition, the current electrochemical characterizations in this study were at room temperature; the performance of electrode materials in lithium-ion batteries at high temperatures is a critical aspect to consider. It is widely recognized that high temperatures

can accelerate undesired side reactions such as electrolyte decomposition, electrode degradation, and increased interfacial resistance. These factors can lead to reduced capacity, increased irreversible capacity loss, accelerated capacity fading, and decreased cycling stability of the battery. Moreover, the higher operating temperatures can also affect the structural integrity of the electrode material, leading to morphological changes, phase transformations, and altered lithium-ion diffusion pathways. These effects can further influence the overall performance and lifespan of the battery. In the future, the behavior of the materials at high temperatures should be carefully investigated and evaluated to ensure the reliability and safety of lithium-ion batteries in real-world applications.

**Author Contributions:** Conceptualization, G.W. and X.T.; methodology, X.Z.; software, F.L. and B.Y.; validation, M.G., J.T., S.H. and G.W.; formal analysis, X.Z.; investigation, G.W. and X.T.; resources, G.W.; data curation, F.L. and B.Y.; writing—original draft preparation, F.L. and B.Y.; writing—review and editing, S.H., G.W. and X.T.; visualization, X.T.; supervision, X.T. and G.W.; project administration, X.T. and G.W.; funding acquisition, S.H., G.W. and X.T. All authors have read and agreed to the published version of the manuscript.

**Funding:** This study was accomplished with financial support by the Youth Science and Technology Talent Growth Program of Guizhou Provincial Education Department (no. QianjiaoheKY [2021]295), Youth Innovation Promotion Association of Chinese Academy of Sciences (2023341).

**Data Availability Statement:** All raw data in this study can be provided by the corresponding authors on request.

**Conflicts of Interest:** The authors declare no conflict of interest.

## References

1. Wang, K.; Hua, W.; Huang, X.; Stenzel, D.; Wang, J.; Ding, Z.; Cui, Y.; Wang, Q.; Ehrenberg, H.; Breitung, B.; et al. Synergy of cations in high entropy oxide lithium ion battery anode. *Nat. Commun.* **2023**, *14*, 1487. [CrossRef]
2. Molaiyan, P.; Dos Reis, G.S.; Karuppiyah, D.; Subramaniyam, C.M.; García-Alvarado, F.; Lassi, U. Recent Progress in Biomass-Derived Carbon Materials for Li-Ion and Na-Ion Batteries—A Review. *Batteries* **2023**, *9*, 116. [CrossRef]
3. Pavlovskii, A.A.; Pushnitsa, K.; Kosenko, A.; Novikov, P.; Popovich, A.A. Organic Anode Materials for Lithium-Ion Batteries: Recent Progress and Challenges. *Materials* **2022**, *16*, 177. [CrossRef] [PubMed]
4. Deng, F.; Zhang, Y.; Yu, Y. Conductive Metal–Organic Frameworks for Rechargeable Lithium Batteries. *Batteries* **2023**, *9*, 109. [CrossRef]
5. Nzereogu, P.U.; Omah, A.D.; Ezema, F.I.; Iwuoha, E.I.; Nwanya, A.C. Anode materials for lithium-ion batteries: A review. *Appl. Surf. Sci. Adv.* **2022**, *9*, 100233. [CrossRef]
6. Wang, C.; Yang, C.; Zheng, Z. Toward Practical High-Energy and High-Power Lithium Battery Anodes: Present and Future. *Adv. Sci.* **2022**, *9*, e2105213. [CrossRef] [PubMed]
7. Zhao, Y.; Li, X.; Yan, B.; Xiong, D.; Li, D.; Lawes, S.; Sun, X. Recent Developments and Understanding of Novel Mixed Transition-Metal Oxides as Anodes in Lithium Ion Batteries. *Adv. Energy Mater.* **2016**, *6*, 1502175. [CrossRef]
8. Roy, K.; Mishra, A.; Nayak, S.; Gupta, P.; Jena, B.B.; Bedanta, S. Spin to Charge Conversion in Semiconducting Antiferromagnetic  $\text{Co}_3\text{O}_4$ . *ACS Appl. Electron. Mater.* **2023**, *5*, 1575–1580. [CrossRef]
9. Ishibe, T.; Maeda, Y.; Terada, T.; Naruse, N.; Mera, Y.; Kobayashi, E.; Nakamura, Y. Resistive switching memory performance in oxide hetero-nanocrystals with well-controlled interfaces. *Sci. Technol. Adv. Mater.* **2020**, *21*, 195–204. [CrossRef]
10. Zhu, J.; Ding, Y.; Ma, Z.; Tang, W.; Chen, X.; Lu, Y. Recent Progress on Nanostructured Transition Metal Oxides As Anode Materials for Lithium-Ion Batteries. *J. Electron. Mater.* **2022**, *51*, 3391–3417. [CrossRef]
11. Manthiram, A. A reflection on lithium-ion battery cathode chemistry. *Nat. Commun.* **2020**, *11*, 1550. [CrossRef]
12. Yu, L.; Zhang, L.; Wu, H.B.; Zhang, G.; Lou, X.W. Controlled synthesis of hierarchical  $\text{Co}_x\text{Mn}_{3-x}\text{O}_4$  array micro-/nanostructures with tunable morphology and composition as integrated electrodes for lithium-ion batteries. *Energy Environ. Sci.* **2013**, *6*, 2664–2671. [CrossRef]
13. Deng, Y.; Wan, L.; Xie, Y.; Qin, X.; Chen, G. Recent advances in Mn-based oxides as anode materials for lithium ion batteries. *RSC Adv.* **2014**, *4*, 23914–23935. [CrossRef]
14. Hu, L.; Zhong, H.; Zheng, X.; Huang, Y.; Zhang, P.; Chen, Q.  $\text{CoMn}_2\text{O}_4$  spinel hierarchical microspheres assembled with porous nanosheets as stable anodes for lithium-ion batteries. *Sci. Rep.* **2012**, *2*, 986. [CrossRef]
15. Zhang, Y.; Gao, W.; Ji, S.; Jia, N. A unique nanosheet assembled  $\text{CoMn}_2\text{O}_4$  hollow nanospheres as superior cyclability anode materials for lithium-ion batteries. *J. Alloys Compd.* **2019**, *786*, 428–433. [CrossRef]

16. Zhang, L.-X.; Wang, Y.-L.; Jiu, H.-F.; Zheng, W.-H.; Chang, J.-X.; He, G.-F. Controllable synthesis of spinel nano-CoMn<sub>2</sub>O<sub>4</sub> via a solvothermal carbon templating method and its application in lithium ion batteries. *Electrochim. Acta* **2015**, *182*, 550–558. [[CrossRef](#)]
17. Yang, G.; Xu, X.; Yan, W.; Yang, H.; Ding, S. Single-spinneret electrospinning fabrication of CoMn<sub>2</sub>O<sub>4</sub> hollow nanofibers with excellent performance in lithium-ion batteries. *Electrochimica Acta* **2014**, *137*, 462–469. [[CrossRef](#)]
18. Sanad, M.M.S.; Yousef, A.K.; Rashad, M.M.; Nagggar, A.H.; El-Sayed, A.Y. Robust and facile strategy for tailoring CoMn<sub>2</sub>O<sub>4</sub> and MnCo<sub>2</sub>O<sub>4</sub> structures as high capacity anodes for Li-ions batteries. *Phys. B Condens. Matter* **2020**, *579*, 411889. [[CrossRef](#)]
19. Zhou, L.; Zhao, D.; Lou, X.W. Double-shelled CoMn<sub>2</sub>O<sub>4</sub> hollow microcubes as high-capacity anodes for lithium-ion batteries. *Adv. Mater.* **2012**, *24*, 745–748. [[CrossRef](#)]
20. Zhang, C.; Zheng, B.; Huang, C.; Li, Y.; Wang, J.; Tang, S.; Deng, M.; Du, Y. Heterostructural Three-Dimensional Reduced Graphene Oxide/CoMn<sub>2</sub>O<sub>4</sub> Nanosheets toward a Wide-Potential Window for High-Performance Supercapacitors. *ACS Appl. Energy Mater.* **2019**, *2*, 5219–5230. [[CrossRef](#)]
21. Alagar, S.; Kumari, S.; Upreti, D.; Aashi; Bagchi, V. High-Performance Mg-Ion Supercapacitor Designed with a N-Doped Graphene Wrapped CoMn<sub>2</sub>O<sub>4</sub> and Porous Carbon Spheres. *Energy Fuels* **2022**, *36*, 14442–14452. [[CrossRef](#)]
22. Ma, Y.; Zhang, L.; Yan, Z.; Cheng, B.; Yu, J.; Liu, T. Sandwich-Shell Structured CoMn<sub>2</sub>O<sub>4</sub>/C Hollow Nanospheres for Performance-Enhanced Sodium-Ion Hybrid Supercapacitor. *Adv. Energy Mater.* **2022**, *12*, 2103820. [[CrossRef](#)]
23. Cai, D.; Qu, B.; Li, Q.; Zhan, H.; Wang, T. Reduced graphene oxide uniformly anchored with ultrafine CoMn<sub>2</sub>O<sub>4</sub> nanoparticles as advance anode materials for lithium and sodium storage. *J. Alloys Compd.* **2017**, *716*, 30–36. [[CrossRef](#)]
24. Ren, F.; Wang, T.; Liu, H.; Liu, D.; Zhong, R.; You, C.; Zhang, W.; Lv, S.; Liu, S.; Zhu, H.; et al. CoMn<sub>2</sub>O<sub>4</sub> nanoparticles embed in graphene oxide aerogel with three-dimensional network for practical application prospects of oxytetracycline degradation. *Sep. Purif. Technol.* **2021**, *259*, 118179. [[CrossRef](#)]
25. Zhang, J.; Yu, A. Nanostructured transition metal oxides as advanced anodes for lithium-ion batteries. *Sci. Bull.* **2015**, *60*, 823–838. [[CrossRef](#)]
26. Luo, S.; Yao, M.; Lei, S.; Yan, P.; Wei, X.; Wang, X.; Liu, L.; Niu, Z. Freestanding reduced graphene oxide-sulfur composite films for highly stable lithium-sulfur batteries. *Nanoscale* **2017**, *9*, 4646–4651. [[CrossRef](#)]
27. Zhang, L.; He, G.; Lei, S.; Qi, G.; Jiu, H.; Wang, J. Hierarchical hollow microflowers constructed from mesoporous single crystalline CoMn<sub>2</sub>O<sub>4</sub> nanosheets for high performance anode of lithium ion battery. *J. Power Source* **2016**, *326*, 505–513. [[CrossRef](#)]
28. Tong, X.; Wang, H.; Wang, G.; Wan, L.; Ren, Z.; Bai, J.; Bai, J. Controllable synthesis of graphene sheets with different numbers of layers and effect of the number of graphene layers on the specific capacity of anode material in lithium-ion batteries. *J. Solid State Chem.* **2011**, *184*, 982–989. [[CrossRef](#)]

**Disclaimer/Publisher’s Note:** The statements, opinions and data contained in all publications are solely those of the individual author(s) and contributor(s) and not of MDPI and/or the editor(s). MDPI and/or the editor(s) disclaim responsibility for any injury to people or property resulting from any ideas, methods, instructions or products referred to in the content.